Heliyon

Received:
18 August 2018
Revised:
12 October 2018
Accepted:
23 April 2019

Cite as: C. Usha, R. Santhakumari, Lynnette Joseph, D. Sajan, R. Meenakshi, A. Sinthiya. Growth and combined experimental and quantum chemical study of glycyl-L-Valine crystal. Heliyon 5 (2019) e01574.
doi: 10.1016/j.heliyon.2019.e01574

Growth and combined experimental and quantum chemical study of glycyl-L-Valine crystal

C. Usha [a], R. Santhakumari [b,*], Lynnette Joseph [c], D. Sajan [c], R. Meenakshi [d], A. Sinthiya [e]

[a] *Department of Physics, J.J. College of Arts and Science (Autonomous), Sivapuram, Pudukkottai, 622 422, Tamil Nadu, India*

[b] *Department of Physics, Government Arts College for Women (Autonomous), Pudukkottai, 622 001, Tamil Nadu, India*

[c] *Department of Physics, Bishop Moore College, Mavelikara, Alappuzha, Kerala, 690 110, India*

[d] *Department of Physics, Cauvery College for Women (Autonomous), Tiruchirappalli, 620 018, Tamil Nadu, India*

[e] *Department of Physics, Srimad Andavan Arts and Science College (Autonomous), Tiruchirappalli, 620 005, Tamil Nadu, India*

[*] Corresponding author.
E-mail address: santhasrinithi@yahoo.co.in (R. Santhakumari).

Abstract

Glycyl-L-Valine (GLV) crystals were grown using distilled water as the solvent at room temperature by solution growth technique. Powder X-ray diffraction confirms the crystalline quality of GLV crystal. The molecular structure of GLV crystal was identified by ^{13}C NMR spectral studies. The nonlinear optical (NLO) behavior of the crystal was found to be ~4.3 times greater than that of potassium dihydrogen orthophosphate. FT-Raman and FT-IR spectra of the GLV were recorded and complete functional group assignment of the determined vibrational bands of GLV have been reported. Density functional theoretical method (DFT) was performed using B3LYP with the 6-311+G (d, p) basis set and the results were compared with the experimental values which confirm the intermolecular interactions responsible for the enhanced NLO activity of the molecule, as evident from NBO and Hirshfeld analyses. The calculated HOMO and LUMO

https://doi.org/10.1016/j.heliyon.2019.e01574

energies show that charge transfer occurs within the molecule. In addition, the molecular electrostatic potential (MEP) analysis, Mulliken atomic charges of the GLV molecule has been investigated using theoretical calculations.

Keywords: Molecular physics, Organic chemistry

1. Introduction

Nonlinear optical (NLO) materials have received abundant attention because of their applications in optoelectronics, such as second harmonic generation (SHG), high data storage optical switching and electro-optic modulation [1]. Recently the analyses of organic nonlinear optical materials have attracted a good attention because of their applications in optoelectronic devices. They have inherent ultra fast response time and large optical susceptibilities as compared with inorganic materials [2, 3]. One of the advantages in working with organic materials is that they allow to have the desired chemical structure and hence the properties for the required nonlinear optical applications [4]. Amino-acid family single crystals have been well-established as really possible second-order NLO materials [5, 6, 7]. Amino acids are fascinating materials for NLO applications as they possess deprotonated carboxylic acid group (COO^{-}) and protonated amino group (NH_3^{+}). Due to this couple nature, amino acids have physical properties that build them ideal candidates for NLO applications [8]. Amino acids are essential building blocks of a range of commercial, environmental and biological applications, since it is the basic blocks of all proteins [9, 10, 11, 12]. The crystal structure of glycyl-L-Valine (GLV) crystal was reported by C. H. Gorbitz et.al. [13]. Based on these information, steps have been taken to grow glycyl-L-Valine (GLV) single crystal by slow evaporation method. The grown crystal has been subjected to Powder X-ray diffraction analysis, NLO studies, Hirshfeld surface analysis, FT-IR, FT-Raman, ^{13}C NMR spectral analysis, Natural Bond Orbital analysis (NBO), Frontier Molecular Orbital (FMO), Global Chemical Reactivity Descriptors analyses, Mulliken Atomic charge analysis, Molecular electrostatic potential analysis.

2. Experimental

2.1. Growth of GLV single crystals

Single crystals of glycyl-L-Valine were grown by slow evaporation method from aqueous solution. glycyl-L-Valine was dissolved in double distilled water. The prepared solution was stirred well and taken in a beaker and the mouth was closed with the perforated lid in order to control the rate of evaporation and kept in room temperature for crystallization. To grow bulk crystal, saturated solution of GLV for 100ml was prepared and kept for crystallization. A crystal of size 4 mm $\times$ 4 mm $\times$ 3mm was obtained in a growth period of 20 days and is shown in Fig. 1.

https://doi.org/10.1016/j.heliyon.2019.e01574

Fig. 1. As grown single crystal of GLV.

2.2. Instrumentation

The Powder X-ray diffraction studies have been performed on PW3071/xx Bracket automated X-ray powder diffractometer. The experimental settings employed in reading the pattern were as follows: The tube current was 30 mA; the operating target voltage was 40 kV; The X-ray from Anode material (Cu) target was filtered monochromatic Kα line of wavelength 1.5406 Å was obtained. The X-ray diffraction indicates the crystalline nature of the GLV crystal. The samples were scanned for 2h values from 10^{o} to 80^{o} at a rate of 2^{o} min^{-1}.

The carbon NMR (^{13}C) spectral analysis was carried out on the GLV crystal in D_2O using Bruker AC200-NMR Spectrometer.

The FT-IR spectrum of the compound was recorded in Bruker IFS 66V spectrometer in the range of 4000−400 cm^{-1} using KBr pellet technique. The spectral resolution is ±2 cm^{-1}. The FT-Raman spectrum of GLV is also recorded in the same instrument with FRA 106 Raman module equipped with Nd:YAG laser source operating at 1.064 μm line widths with 200 mW power. The spectra are recorded in the range of 4000−100 cm^{-1} with scanning speed of 30 cm^{-1} min^{-1} of spectral width 2 cm^{-1}.

Kurtz and Perry [14] second harmonic generation (SHG) test was conducted on GLV crystal in order to understand the NLO behavior of the crystal. The powder form of GLV crystal was taken in a micro capillary tube and was illuminated using Spectra Physics Quanta Ray DHS2. Nd:YAG laser using the first harmonics output of 1064 nm with pulse width of 8 ns and repetition rate 10 Hz and its NLO efficiency was measured with potassium dihydrogen orthophosphate (KDP), as a reference material. The input laser energy incident on the powdered sample was chosen to be 3.4 mJ.

https://doi.org/10.1016/j.heliyon.2019.e01574

3. Theory/Calculation

Density Functional Theory (DFT) with the hybrid functional (B3LYP) with the 6-311+G (d, p) basis set have been employed to calculate optimized bond lengths, bond angles, dihedral angles, atomic charges, vibrational wavenumbers with their IR intensities and Raman scattering activities. All these calculations were performed using Gaussian 09 program [15]. The natural bonding orbitals (NBO) calculations were performed using NBO 5.1 program as implemented in the Gaussian 09 package. The electrophilic and nucleophilic attacks of GLV were presented on molecular electrostatic potential (MEP) and electronic properties have been deduced from HOMO−LUMO analysis.

4. Results and discussion

4.1. Powder X-ray diffraction analysis

Comparison between the PXRD patterns of the GLV with the single XRD patterns revealed the exact identities of the grown GLV crystal which can be seen from Fig. 2. The lattice parameters are evaluated for GLV as a = 5.5238(7)Å, b = 26.581(3)Å and c = 44.093(5)Å with space group $P2_12_12_1$. The calculated lattice parameters from the PXRD are in good agreement with the reported values [13].

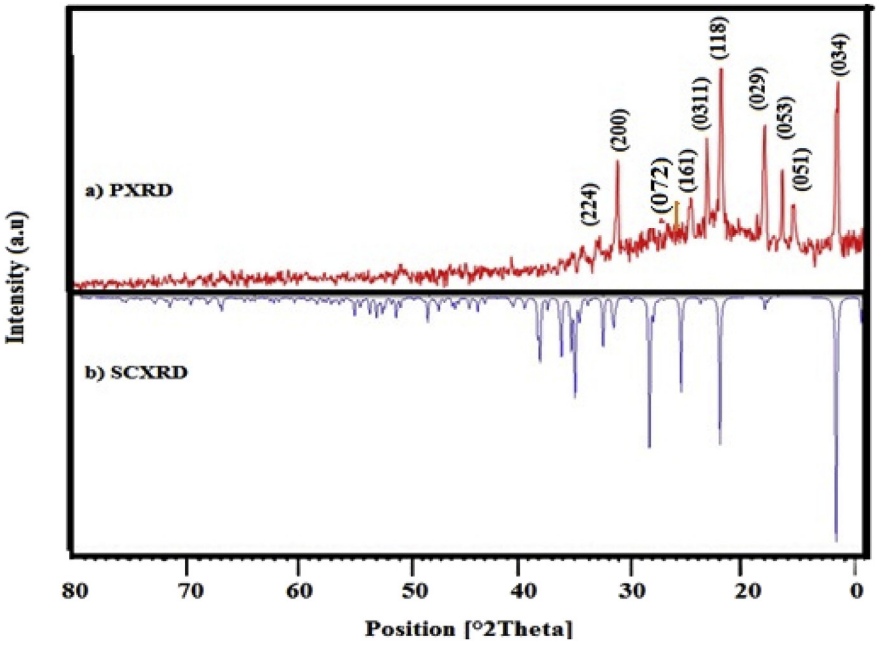

Fig. 2. (a) PXRD (b) SCXRD data of the GLV generated (Ref. [13]) using the Mercury 3.0 program.

https://doi.org/10.1016/j.heliyon.2019.e01574

4.2. ^{13}C NMR spectral analysis of GLV single crystal

In Fig. 3. ^{13}C-NMR spectrum, GLV exhibits seven signals with respect to seven carbon atoms of different chemical environment. The signals at δ =17.0 ppm and at δ= 18.75 ppm are attributed to the two methyl groups of glycyl-l-valine respectively. The peak at δ= 40.33 ppm is due to amino group of GLV. The peak at δ = 60.99 ppm for GLV is due to tertiary carbon connected to amino group. The signal (CH) at δ = 29.98 ppm is integrated for one carbon due to presence of carboxylic acid isopropyl carbon. Two peaks with different intensities at δ = 178.33 ppm and at δ = 166.55 ppm respectively were found due to the presence of carbonyl carbons of two COOH groups present in the GLV crystal [14, 15]. The chemical shift values of GLV with assignments are stacked in Table 1.

4.3. Nonlinear optical behavior of GLV single crystal

Powder SHG efficiency of GLV crystal is found to be about ~4.3 times that of potassium dihydrogen orthophosphate crystal [16].

4.4. Optimized geometry and Hirshfeld surface analyses

The optimized structure of the molecule is shown in Fig. 4 and the geometric parameters are given in Table 2. The zero point vibrational energy of the compound in DFT (B3LYP) with 6-311+G(d,p) is 137.70 kcal/mol. The bond length between C_3-C_4 and C_3-C_7 are nearly equal since both C are balanced by N–H and CH_3 in the chain. The bond lengths of C_4-C_5 and C_4-C_6 are nearly equal due to the balance of CH_3 groups in the chain. However the decrease in the experimental values of C_1-C_2-N_9, C_4-C_3-C_7 and C_2-N_9-C_3 bond angles (115.6̊, 108.7̊ and 121.0̊) from the DFT values (118.05̊, 111.58̊ and 129.24̊) as well as the increase in N_9-C_2-O_{10}, C_3-C_7-O_{12} and O_{11}-C_7-O_{12} (123.6̊, 117.0̊ and 125.7̊) from DFT values (120.19̊, 112.14̊

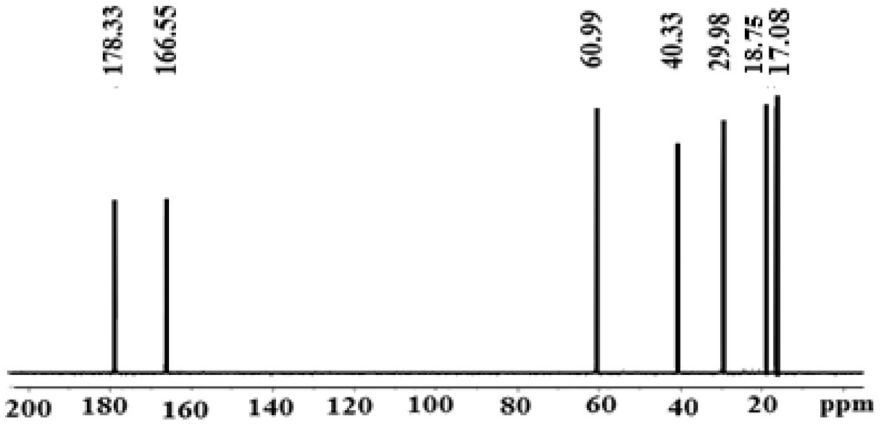

Fig. 3. ^{13}C NMR spectrum of GLV single crystal.

https://doi.org/10.1016/j.heliyon.2019.e01574

Table 1. The chemicals shift in ^{13}C NMR spectrum of GLV single crystal.

Chemical shift (ppm)	Group identification
17.08& 18.75	– (CH_3)
29.98	– CH– (isopropyl)
40.33	– NH_2
60.99	– CH_2–
166.55	Amide carboxyl
178.33	Acid carboxyl

and 123.07̊) clearly suggests a rearrangement in the structure leading to considerable reduction in periodicity during crystallization. It is seen that DFT calculation predicts C_7=O_{11} bond length to be 1.2064 Å, while the corresponding experimental value is 1.254 Å, which gives evidence for the existence of intermolecular N_9-H_{26}….O_{11} and N-H…O bonds involving amino group as well. Further it is evident that the C_7-O_{12} bond length is decreased by 0.103 Å in XRD than the corresponding DFT value. The decrease in C_7-O_{12} and increase in C_7=O_{11} bond length in XRD values affirm the deprotonation of the carboxylate group and the protonation of the amino group. It is observed that C_2=O_{10} bond length is elongated in XRD (1.2306 Å) than the calculated value (1.2186 Å) which reveals the decrease in its double bond character in the amide group as a result of hydrogen bond formation at C=O sites.

In the case of molecular crystals, the intermolecular hydrogen bonding and the packing modes can be depicted using the Hirshfeld surface. Crystal explorer version 3.0 [17] software was used to plot the Hirshfeld surface and finger print plots of GLV singe crystal. The Hirshfeld surface analysis gives the graphical explanation for efficient packing to complete with hydrogen bonding as structure-directing process (Fig. 5a,b,c,d). The crystal system is stabilized using N-H…O, C-H…O hydrogen

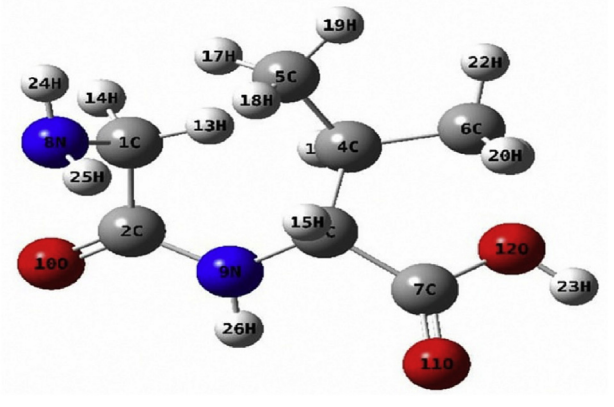

Fig. 4. Molecular Structure of GLV single crystal.

https://doi.org/10.1016/j.heliyon.2019.e01574

Table 2. Optimized geometric parameters of GLV single crystal.

Bond Length in Å			Bond Angles in degrees			Dihedral Angles in degrees		
Parameter	**XRD [13]**	**B3LYP /6-311+ G (d,p)**	**Parameter**	**XRD [13]**	**B3LYP /6-311+ G (d,p)**	**Parameter**	**XRD [13]**	**B3LYP/6-311+ G (d,p)**
C_1-C_2	1.505(7)	1.532	C_2-C_1-N_8	109.5(4)	111.0	H_{26}-N_9-C_3-H_{15}	-124.7	167.24
C_1-C_8	1.480(6)	1.466	C_2-C_1-H_{13}	109.8	110.2	H_{25}-N_8-C_1-H_{13}	129.8	-161.63
C_1-H_{13}	0.990	1.102	C_2-C_1-H_{14}	109.9	104.7	H_{24}-N_8-C_1-H_{14}	11.1	-39.68
C_1-H_{14}	0.989	1.089	C_1-C_2-N_9	115.6(4)	118.1	H_{24}-N_8-C_1-C_2	-109.6	-154.24
C_2-N_9	1.336(6)	1.377	C_1-C_2-O_{10}	120.9(4)	121.8	H_{25}-N_8-C_1-H_{13}	-109.0	-161.63
C_2-H_{10}	1.230(6)	1.219	N_8-C_1-H_{13}	109.6	114.4	H_{26}-N_9-C_3-C_4	-7.8	47.70
C_3-C_4	1.534(6)	1.550	N_8-C_1-H_{14}	109.9	108.6	H_{26}-N_9-C_3-C_7	116.7	-77.64
C_3-C_7	1.535(7)	1.531	C_1-N_8-H_{24}	109.5	110.9	C_2-N_9-C_3-H_{15}	55.3	-19.52
C_3-C_9	1.452(6)	1.455	C_1-N_8-H_{25}	109.5	113.5	C_2-N_9-C_3-C_4	172.3	-139.06
C_3-H_{15}	1.001	1.091	H_{13}-C_1-H_{14}	108.2	107.4	C_2-N_9-C_3-C_7	-63.2	95.59
C_4-C_5	1.518(8)	1.534	N_9-C_2-O_{10}	123.6(5)	120.2	N_8-C_1-C_2-N_8	149.7(4)	-75.637
C_4-C_6	1.518(9)	1.535	C_2-N_9-C_3	121.0(4)	129.2	H_{11}-C_1-C_2-O_{10}	89.5	-127.42
C_4-H_{16}	1.001	1.097	C_2-N_9-H_{26}	119.4	113.4			
C_4-H_{17}	0.981	1.091	C_4-C_3-C_7	112.5(4)	112.3			
C_5-H_{18}	0.978	1.095	C_4-C_3-N_9	108.7(4)	111.6			
C_5-H_{19}	0.979	1.093	C_4-C_3-H_{15}	108.0	108.4			
C_6-H_{20}	0.981	1.095	C_3-C_4-C_5	110.4(4)	110.6			
C_6-H_{21}	0.978	1.093	C_3-C_4-C_6	112.8(4)	111.3			
C_6-H_{22}	0.980	1.093	C_3-C_4-H_{16}	107.6	107.0			
C_7-O_{11}	1.247(6)	1.206	C_7-C_3-N_9	111.4(4)	110.1			
C_7-O_{12}	1.254(6)	1.350	C_7-C_3-H_{15}	108.1	105.5			
N_8-H_{24}	0.910	1.012	C_3-C_7-0_{11}	117.0(4)	124.8			
N_8-H_{25}	0.911	1.014	C_3-C_7-O_{12}	117.3(4)	112.1			
N_9- H_{26}	0.880	1.013	N_9-C_3-H_{15}	108.0	108.7			
			C_3-N_9-H_{26}	119.4	117.1			
			C_5-C_4-C_6	110.7(5)	110.9			
			C_5-C_4-H_{16}	107.6	108.7			
			C_4-C_5-H_{17}	109.4	112.0			
			C_4-C_5-H_{18}	109.4	110.9			
			C_4-C_5-H_{19}	109.5	110.2			
			C_6-C_4-H_{16}	107.5	108.2			
			C_4-C_6-H_{20}	109.4	111.1			
			C_4-C_6-H_{21}	109.5	112.4			
			C_4-C_6-H_{22}	109.4	110.1			
			H_{17}-C_5-H_{18}	109.5	108.0			

(*continued on next page*)

https://doi.org/10.1016/j.heliyon.2019.e01574

Table 2. (*Continued*)

Bond Length in Å			Bond Angles in degrees			Dihedral Angles in degrees		
Parameter	**XRD [13]**	**B3LYP /6-311+ G (d,p)**	**Parameter**	**XRD [13]**	**B3LYP /6-311+ G (d,p)**	**Parameter**	**XRD [13]**	**B3LYP/6-311+ G (d,p)**
			H_{17}-C_5-H_{19}	109.5	108.0			
			H_{18}-C_5-H_{19}	109.5	107.6			
			H_{20}-C_6-H_{21}	109.4	107.9			
			H_{20}-C_6-H_{22}	09.5	107.7			
			H_{21}-C_6-H_{22}	109.6	107.4			
			0_{11}-C_7-0_{12}	125.7(5)	123.1			
			H_{24}-N_8-H_{25}	109.5	108.2			

bonding with R_2^2 (11), R_3^3(12) and R_3^2(9) graph set and it is shown in Fig. 5a. Hirshfeld surface analysis revealed the dominance of H...H interactions (55.7% in overall surface) indicating that structure is also stabilized by Van der Walls contacts, and their contribution are consistent with the description of molecular packing. In Fig. 5b. The red spot indicates the weak C—H···O interaction and Fig. 5c show the overall two-dimensional fingerprint plots. The Hirshfeld surfaces mapped with

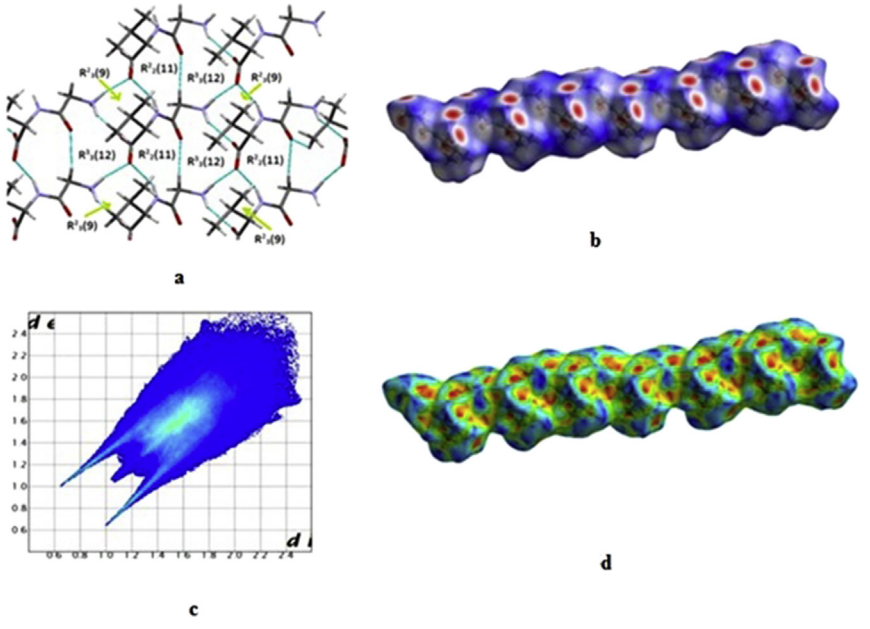

Fig. 5. (a) Packing fraction of GLV single crystal. (b) Hirshfeld surfaces for GLV single crystal. (c) The breakdown of the fingerprint plot for GLV single crystal. (d) Shaped type Hirshfeld surfaces for GLV single crystal.

https://doi.org/10.1016/j.heliyon.2019.e01574

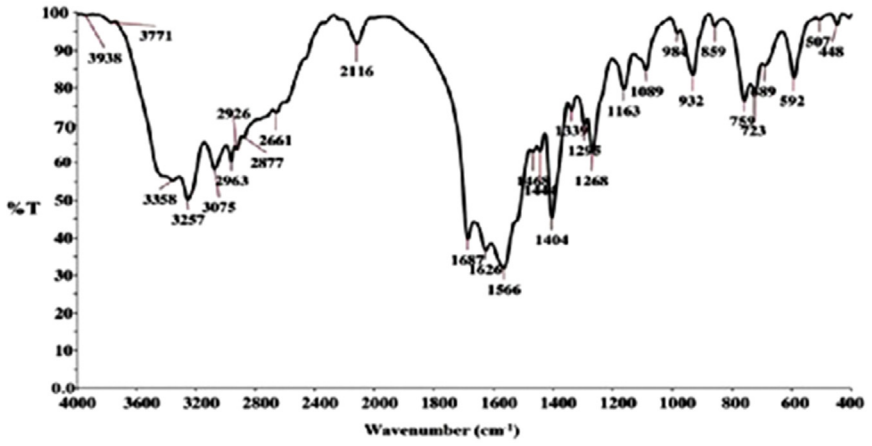

Fig. 6. FT-IR spectrum of GLV single crystal.

the shape index property with the bright-red spot Fig. 5d indicate the C—H···O interaction.

4.5. FT-IR and FT-Raman spectral analyses

Experimental spectra of FTIR and FT-Raman are presented in the Figs. 6 and 7 respectively. The observed (FT-IR and FT-Raman), calculated vibrational frequencies and vibrational assignments are given in Table 3.

4.5.1. Methyl group vibrations

The side chain of GLV has two methyl groups attached to the C atom. The CH_3 stretching and deformation vibrations are more or less localized, and offer to good group frequencies. The positions of the C-H stretching vibrations are among the most stable in the spectrum, since the CH_3 group also exhibit C_S symmetry. In aliphatic compounds, the asymmetric and symmetric CH_3 stretching vibrations are normally observed in the region 2950- 2850 cm-1 [18, 19, 20]. In the present compound, the CH_3 asymmetric stretching mode of vibration appears at 2963 cm^{-1} and 2958 cm^{-1} in the FT-IR and FT-Raman spectrum respectively. The strong Raman band at 2872 cm^{-1} and a medium band in IR at 2877 cm^{-1} are assigned to methyl symmetric stretching mode.

The asymmetric and symmetric bending vibrations of methyl groups normally appear in the region 1465-1410 cm^{-1} and 1390-1370 cm^{-1} respectively. The asymmetric bending mode is observed as a medium and broad band at 1444 cm^{-1} in IR and as a medium band at 1406 cm^{-1} in Raman, while the symmetric bending mode is observed as a weak band at 1339 cm^{-1} in both IR and Raman.

https://doi.org/10.1016/j.heliyon.2019.e01574

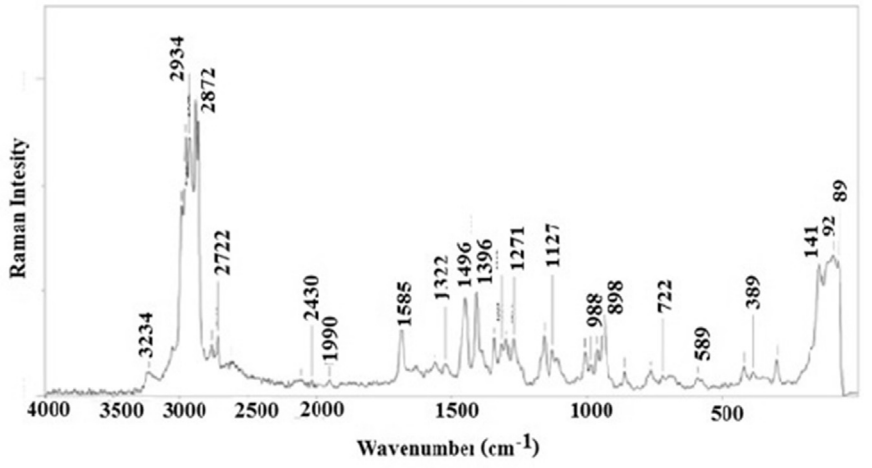

Fig. 7. FT-Raman spectrum of GLV single crystal.

4.5.2. Amino group vibrations

The NH, group in both primary amines and amides is associated with three characteristic infrared absorption bands. Two, with frequencies around 3500 and 3300 $cm^{-1,}$ are identified respectively with the antisymmetric and symmetric NH stretching vibrations. in the third, in the range 1590−1650 cm^{-1}, the HNH bending mode is considered to predominate [21]. In this present case, the N-H stretching frequencies are observed at 3358 cm^{-1} and 3075 cm^{-1} in the FT-IR are assigned to asymmetric and symmetric vibration respectively. The observed blue shifting of amino stretching wave numbers clearly demonstrates the participation of amino group in intermolecular hydrogen bond formation. The HNH symmetric deformation wave numbers are found at 1566 and 1559 cm^{-1} in the FT-IR and FT-Raman spectrum respectively.

4.5.3. COOH group vibrations

Free amino acids also have carboxylate ion (COO^- ion) stretching vibrations, a strong band occurring in the region 1600-1560 cm^{-1} [22, 23]. In FT-IR and FT-Raman, a strong band observed at 1687 $cm^{-1}$and 1685 cm^{-1} are due to the C=O stretching of the COOH group. The red shifting of this wave number suggests a decrease in its double bond character which establishes the existence of intermolecular N–H…O bonds within the molecule.

4.5.4. Amide group vibrations

The C=O band frequency in amides is predominantly sensitive to hydrogen bonding at the C=O group, while the C-N vibration is equally responsive to the state of

https://doi.org/10.1016/j.heliyon.2019.e01574

Table 3. Detailed assignment of fundamental vibrations of GLV single crystal.

DFT scaled	IR expt		Raman expt	Assignment
3498				O_{12}-H_{23} stretch
3355	3358	Sbr		NH_2 asym stretch
3332	3257	Sbr	3224 w	N_9-H_{26} stretch
3275	3075	Sbr	2986 m	NH_2 sym stretch
2905	2963	Sbr	2958 s	methyl asym stretch
2897	2926	Sbr	2934 s	methyl asym stretch
2889				C_3-H_{15} stretch
2886				H_{22}-C_6-H_{21} asy stretch
2879				CH asym stretch
2873				CH asym stretch
2821	2877	Mbr	2872 s	CH sym stretch
2816				CH sym stretch
2810	2661	Mbr	2765 w	C_4-H_{16} stretch
2747	2116	W	2620 w	C_1-H_{13} stretch
1680	1687	S	1685 m	C_7-O_{11} stretch
1630	1626	Vs		C_2-0_{10} stretch
1564	1566	Vs	1559 w	H_{25}-N_8-H_{24} scissoring
1410	1468	Mbr	1446 m	methyl group scissoring
1404	1444	Mbr	1406 m	methyl group asym bend
1399	1404	S		H_{13}-C_1-H_{14} scissoring
1391				methyl group scissoring
1386				methyl group asym bend
1384				C_3-N_9-H_{26} scissoring
1330	1339	W	1339 w	methyl group sym bend
1314			1313 w	H_{13}-C_1-H_{14} wag
1310				methyl group sym bend
1288	1295	M	1296 w	N_9-C_3-C_4-C_6 bend
1273	1268	M	1271 w	H_{13}-C_1-H_{14} asym bend
1261				N_9-C_3-C_4-C_6 bend, H_{13}-C_1-H_{14} asym bend
1258				C_7-O_{12}-H_{23} sym bend
1236				N_9-C_3-C_4-C_6 bendi
1212	1163	W	1157 w	H_{13}-C_1-N_8-H_{24} sym bend
1203				N_9-C_3-C_4-C_6 sym bend
1117			1127 w	H_{23}-O_{12}-C_7-C_3
1108				CH bend sym
1097				CH bend sym
1080	1089	W	1003 w	H_{13}-C_1-H_{14} wag,H_{24}- N_8-H_{25} wag
1044				CH bend asym

(*continued on next page*)

https://doi.org/10.1016/j.heliyon.2019.e01574

Table 3. (*Continued*)

DFT scaled	IR expt		Raman expt	Assignment
1024	984	Vw	984 w	C_3-N_9 stretch
992				C_1-N_8 stretch
912	932	W	939 w	H_{13}-C_1-N_8-H_{24} bend
905				C_6-C_4-C_5 asym bend
890				C_3-C_4-C_6 asym bend
875	859	Vw	860 w	H_{16}-C_4-C_5-C_6 bend
824				C_3-C_4-C_5-C_6 bend
808				C_3-C_4-C_5-C_6 bend, C_3-N_9-C_2 bend
795				H_{13}-C_1-N_8-H_{24} bend
737	759	M	763 vw	H_{25}-N_8-H_{24} wag
701	723	M	722 vw	H_{25}-N_8-H_{24} wag
679	689	W		N_9-C_2-O_{10} wag
600			589 w	H_{23}-O_{12}-C_7-O_{11} wag
579				N_9-C_3-C_4-C_6 bend
557	592	M		N_9-C_3-C_4-C_6 bend
516	507	Vw		N_9-C_3-C_4-C_6 bend
467	448	Vw		H_{12}-C_1-C_2-N_9 bend
430				N_9-C_3-C_7-O_{12} bend
398			387 vw	N_9-C_3-C_7-O_{12} bend
335				N_9-C_3-C_4-C_6 bend
325				C_3-C_4-C_5-C_6 bend
283			300 w	N_9-C_3-C_4-C_6 bend
260				H_{13}-C_1-N_8-H_{24}
239				H_{13}-C_1-N_8-H_{24}
224				H_{13}-C_1-N_8-H_{24}
213				C_3-C_6-C_4-H_{26} bend
196				C_6-C_4-C_5-H_{17} bend
149				N_9-C_2-C_1—H_{14} bend
142			141 s	C_3-C_7-C_4 sciss
105			92 s	N_9-C_2-C_1—H_{14} bend
65			69 s	N_9-C_3-C_4-C_6 bend
57				CCO bend
49				N_9-C_3-C_4-C_6 bend
38				N_9-C_3-C_4-C_6 bend

hydrogen bonding at the C=O and N-H sites [24, 25, 26]. The active fundamentals which appear with medium intensity at 932 cm^{-1} in IR and at 939 cm^{-1} in Raman are identified as C-N stretching vibration [27]. It can be inferred that that hydrogen bonding at the carbonyl sites stabilizes the charged resonance structure of the amide

https://doi.org/10.1016/j.heliyon.2019.e01574

bond. This results in an increase in the C_2-N_9 double bond character as the C_2=O_{10} bond order decreases, there by the C_2-N_9 bond length decreases while the C_2=O_{10} bond lengthens. This charge resonance structure is evident from the natural bond orbital analysis as well, which is responsible for the enhancement of the NLO activity of the molecule.

4.6. Natural bond orbital analysis

The natural bond orbital (NBO) analysis provides an efficient method for investigating conjugative interactions in molecular systems. Stabilizing interactions between filled and unoccupied orbitals and destabilizing interactions between filled orbitals can also be obtained from this analysis [28]. The hyperconjugative interaction energy was deduced from the second-order perturbation approach.

$$E(2) = -n_\sigma \frac{\langle \sigma|F|\sigma\rangle^2}{\varepsilon_{\sigma^*} - \varepsilon_\sigma} = -n_\sigma \frac{F_{ij}{}^2}{\Delta E} \quad (1)$$

where $\langle \sigma|F|\sigma\rangle^2$ or F_{ij}^2 is the Fock matrix element between the ith and jth NBO orbitals, ε_σ and ε_{σ^*} are the energies of σ and σ* NBO's, and n_σ is the population of the donor σ orbital. The greater the $E^{(2)}$value, the more intensive is the interaction between electron donors and acceptors, i.e. the greater the extent of conjugation of the system.

Table 4 shows the most important interactions between Lewis and non-Lewis orbitals with Oxygen lone pairs, the second order perturbation energy values, $E(2)$, corresponding to these interactions, and the overlap integral of each orbital pair.

A very strong interaction has been observed between the p-type orbital containing the lone electron pair of N_9 and the neighbour π* (C_2 - O_{10}) antibonding orbital of the glycine part. This interaction is responsible for a pronounced decrease of

Table 4. Second order perturbation theory analysis of Fock matrix in NBO basis of GLV single crystal.

Donor NBO (i)	Occupancy	Acceptor NBO (j)	Occupancy	Hybrid (%p character)	E(2)[a] kJ/mol	E(j)-E(i)[b] a.u.	F(i,j)[c] a.u
$LP_1(N_9)$	1.72008	$\pi^*(C_2 - O_{10})$	0.01253	$sp^{2.02}$ (66.79)	234.3	0.29	0.115
$LP_2(O_{10})$	1.86832	$\sigma^*(C_1 - C_2)$	0.06992	$sp^{2.74}$(73.21)	80.09	0.62	0.098
$LP_2(O_{10})$	1.86832	$\sigma^*(C_2 - N_9)$	0.07582	$sp^{2.25}$(69.15)	104.4	0.70	0.119
$LP_2(O_{11})$	1.85233	$\sigma^*(C_3 - C_7)$	0.07834	$sp^{3.03}$(75.11)	73.58	0.63	0.096
$LP_2(O_{11})$	1.85233	$\sigma^*(C_7 - O_{12})$	0.09861	$sp^{2.68}$(72.69)	140.7	0.62	0.130
$LP_2(O_{12})$	1.82053	$\pi^*(C_7 - O_{11})$	0.02195	$sp^{1.91}$(65.52)	188.4	0.35	0.113

[a] E(2) means energy of hyperconjugative interactions; cf. Eq. (1.0).

[b] Energy difference between donor and acceptor NBO.

[c] F(i,j) is the Fock matrix element between the donor and acceptor NBO.

https://doi.org/10.1016/j.heliyon.2019.e01574

the lone pair orbital occupancy (1.72008), than the other occupancy (0.01253), and indicates hyperconjugation between N_9 and the valine part. The energy contribution of $LP_2\ O_{11} \rightarrow \sigma^*\ (N_8{-}H_{25})$ value is 2.43 kJ mol^{-1}. This energy value indicate the presence of a weak intramolecular C—H$\cdots$O hydrogen bonding interaction between the oxygen lone pair and the antibonding orbitals.

The contributions of the stabilization energies for the $LP_2\ O_{11} \rightarrow \sigma^*(C_3 - C_7)$ [73.58 kJ mol^{-1}] and $LP_2\ O_{11} \rightarrow \sigma^*(C_7 - O_{12})$ [140.7 kJ mol^{-1}] charge transfers have higher values than the other delocalizations. An important contribution for the molecular stabilization is further given by O_{12} through the overlap of its sp99.9 lone pair $LP_2\ O_{12}$ with the $\pi^*(C_7 - O_{11})$ orbital. This is a consequence of the stabilization of the carboxylate ion by resonance where by the negative charge cloud is delocalized between the two electronegative oxygen atoms in the resonance structure, which leads to the de-protonation of the carboxyl group and the subsequent protonation of the amino group. Intermolecular hydrogen bond at the N-H sites further leads to delocalization of charge cloud through C—H….O, N-H…..O and C —H……N bonds which act as a channel for intermolecular charge transfer. Such D-π-A systems in crystalline form having dense molecular packing serve as a good candidate for high mobility charge transport diode and field effect transistor [29].

4.7. Frontier molecular orbital (FMO) analysis

The frontier molecular orbitals are very much helpful for studying the electric and optical properties of the organic molecules. The stabilization of the bonding molecular orbital and destabilization of the antibonding can increase when the overlap of two orbitals increases. In the molecular interaction, there are the two important orbitals that interact with each other. One is the highest energy occupied molecular orbital is called HOMO represents the ability to donate an electron. The other one is the lowest energy unoccupied molecular orbital is called LUMO as an electron acceptor. These orbitals are sometimes called the frontier orbitals. The interaction between them is much stable and is called filled empty interaction. The charge densities of the HOMO and LUMO are shown in Fig. 8. The HOMO is mainly localized over the entire molecule except amine and a methyl group and the LUMO is spread over the entire molecule except methyl group. The HOMO-1 is concentrated over the CCN, NH_2 and C=O group of the molecule. Molecule with large HOMO−LUMO gap has been shown to be stable and unreactive; those with small gaps are chemically reactive [30, 31, 32, 33, 34]. The HOMO and LUMO energy are -8.7447eV and -3.2005eV in gas phase. The energy difference between HOMO and LUMO orbital is called as energy gap that is a significant stability for structures. The DFT level calculated energy gap is 5.5442eV, show the large energy gap and reflect the zero electrical activity of the molecule.

https://doi.org/10.1016/j.heliyon.2019.e01574

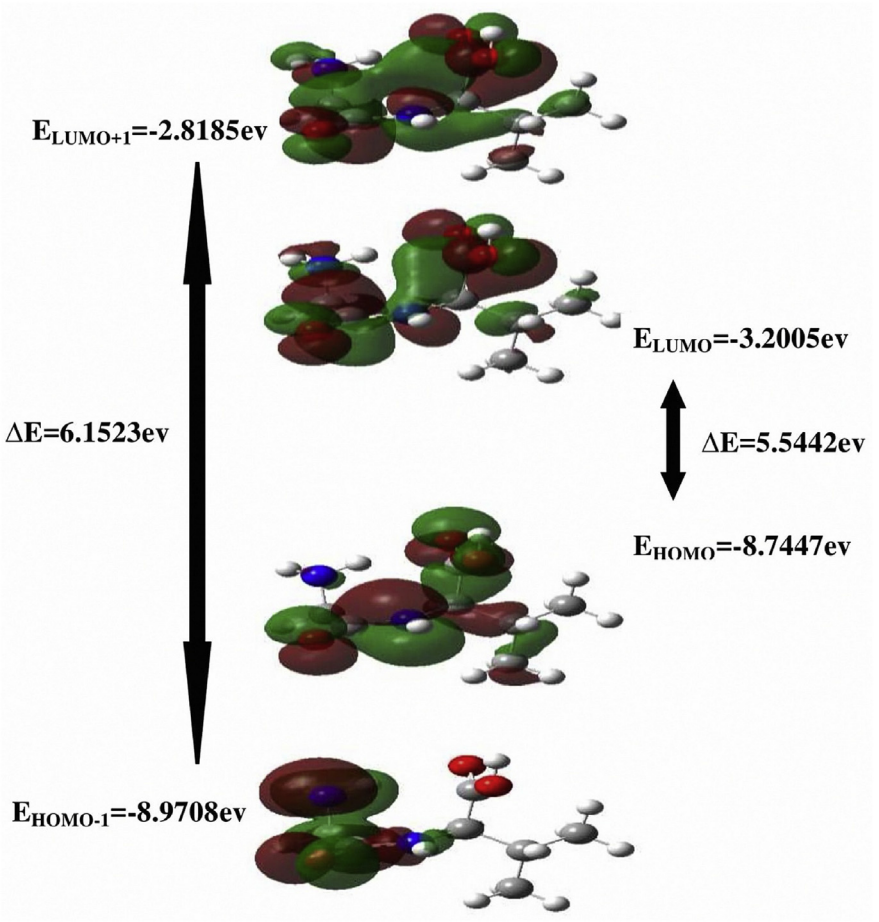

Fig. 8. HOMO, HOMO-1, LUMO and LUMO+1 representation of GLV single crystal.

4.8. Analysis of global chemical reactivity descriptors (GCRD) of GLV single crystal

Global chemical reactivity descriptors are based on the conceptual density functional theory (DFT) and are used to understand the relationship between global chemical reactivity, structure, stability etc. parameters of any molecules. The values of various GCRD parameters such as chemical hardness (η), chemical potential (μ), softness (S), electronegativity (χ) and electrophilicity index (ω) of GLV molecule using HOMO and LUMO energies values using different functional and given in Table 5. An approximation for absolute hardness η was developed [35, 36, 37] as given below:

$$\eta = \frac{I - A}{2} \tag{2}$$

where I is the vertical ionization energy and A is vertical electron affinity.

https://doi.org/10.1016/j.heliyon.2019.e01574

Table 5. Calculated energy values of FMOs, their difference, η, μ, S, χ and ω by B3LYP using/6-31G* basis set for GLV single crystal.

Parameters	B3LYP	
	a.u	e.V
E_{HOMO}	-0.3213	-8.7447
E_{HOMO-1}	.0.3296	-8.9708
E_{LUMO}	-0.1176	-3.2005
E_{LUMO+1}	-0.1035	-2.8185
Δ $E_{HOMO-LUMO}$	0.2037	5.5442
Δ $E_{HOMO-1-LUMO+1}$	0.2260	6.1523
Hardness (η)	0.1018	2.7702
Potential (μ)	-0.2195	-5.9730
Softness (S)	1.5772	42.9187
Electronegativity (χ)	0.2195	5.9730
Electrophilic index (ω)	0.2364	6.4348

As per Koopman's theorem [38] the ionization energy and electron affinity can be specified through HOMO and LUMO orbital energies as:

$$I = - E_{HOMO}$$

$$A = - E_{LUMO}$$

The calculated values of GCRD such as η, μ, S, χ and ω for GLV single crystal are also presented in Table 5. The higher energy of HOMO is corresponds to the more reactive molecule in the reactions with electrophiles, while lower LUMO energy is essential for molecular reactions with nucleophiles [39].

Hence, the hardness of any materials is correspond to the gap between the HOMO and LUMO orbitals. If the energy gap of HOMO-LUMO is larger, than molecule would be harder [36].

$$\eta = \frac{1}{2}(E_{LUMO} - E_{HOMO}) \tag{3}$$

The electronic chemical potential of a molecule is calculated by:

$$\mu = -\left(\frac{I + A}{2}\right) \tag{4}$$

The softness of a molecule is calculated by:

https://doi.org/10.1016/j.heliyon.2019.e01574

$$s = \frac{I}{2\eta} \tag{5}$$

The electronegativity of the molecule is calculated by:

$$\chi = \left(\frac{I + A}{2}\right) \tag{6}$$

The electrophilicity index of the molecule is calculated by:

$$\omega = \frac{\mu^2}{2\eta} \tag{7}$$

4.9. Mulliken atomic charge

Mulliken atomic charge calculation has an important role in the application of quantum chemical calculation to molecular system because of atomic charges effect dipole moment, molecular polarizability, electronic structure and more a lot of properties of molecular systems. The calculated Mulliken charge values of GLV are listed in Table 6. The Mulliken charge distribution of the GLV in B3LYP/6-311+G(d,p) methods is shown in Fig. 9. The charge distribution of the molecule shows all the hydrogen atoms and C2 are positively charged whereas the other carbon atoms are negative. C3, C7 and O12 display strong electonegativity, the theoretical Mulliken atomic charge of C3, C7 and O12 is -0.0916, -0.1419 and -0.1452 a.u respectively.

Table 6. Mulliken atomic charge of GLV single crystal.

Atoms	Charges	Atoms	Charges
C1	-0.17657	H14	0.17376
C2	0.16455	H15	0.17602
C3	-0.09163	H16	0.16279
C4	0.00292	H17	0.16159
C5	-0.51633	H18	0.14188
C6	-0.52334	H19	0.14865
C7	-0.14193	H20	0.15049
N8	-0.43976	H21	0.15114
N9	-0.12986	H22	0.14796
O10	-0.33618	H23	0.27276
O11	-0.24148	H24	0.2366
O12	-0.14529	H25	0.23756
H13	0.12965	H26	0.28407

https://doi.org/10.1016/j.heliyon.2019.e01574

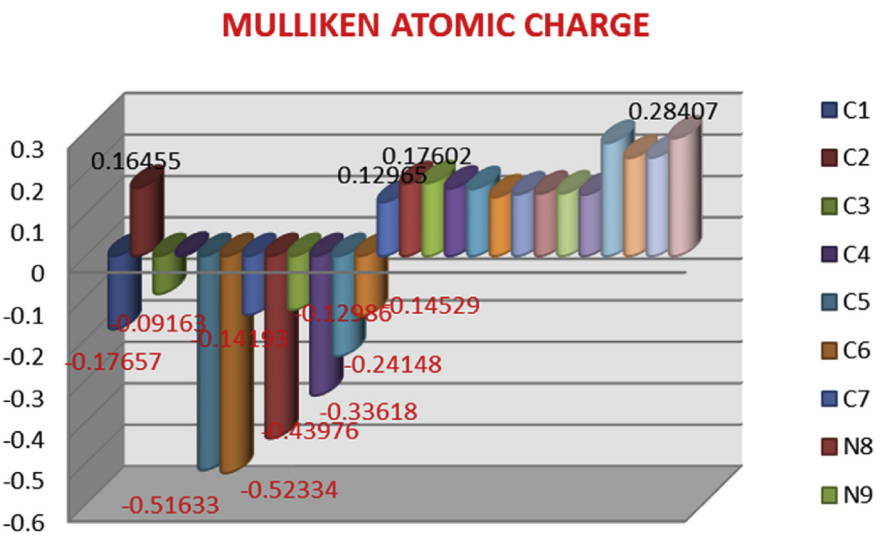

Fig. 9. Mulliken atomic charge of GLV single crystal.

4.10. Molecular electrostatic potential (MEP)

To investigate the reactive sites of 1, the molecular electrostatic potential [40] was evaluated using the B3LYP/6-311G (d,p) method. The molecular electrostatic potential, V(r) at a point 'r' in the space around a molecule (in atomic units) can be expressed as:

$$V(r) = \sum_{A} \frac{z_A}{|R_A - r|} - \int \frac{\rho(r\prime)dr\prime}{r' - r} \tag{8}$$

Where Z_A is the charge on nucleus A, located at R_A, ρ(r') is the electronic density function of the molecule and r' is the dummy integration variable. The first and second terms represent the contributions to the potential due to nuclei and electrons,

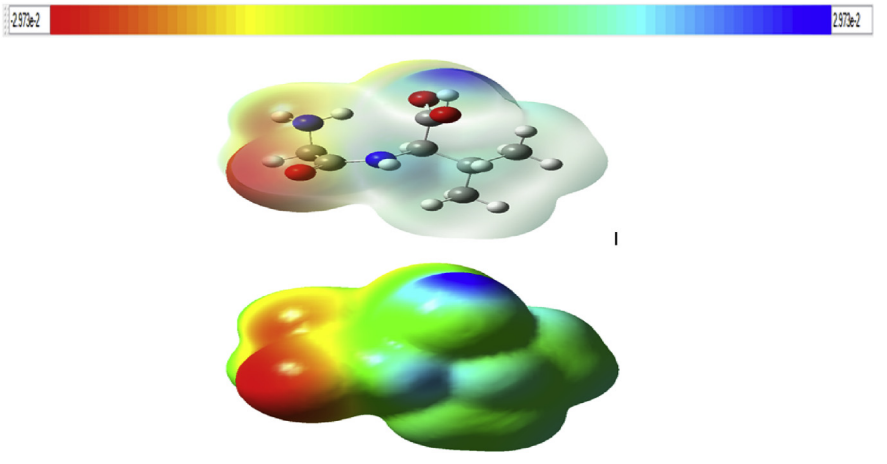

Fig. 10. Molecular electrostatic potential (MEP) map of GLV single crystal.

https://doi.org/10.1016/j.heliyon.2019.e01574

Table 7. Theoretically computed energies (a.u.), zero-point vibrational energies (kcal mol^{-1}), rotational constants (GHz), entropies (cal mol^{-1} K^{-1}) and dipole moment (D) for GLV single crystal.

Parameters	DFT/B3LYP/6-311++G(d,p)
Total energy	-610.564
Zero-point vibrational energy	137.702
Rotational constants	
A	1.114
B	0.689
C	0.549
Entropy	
Total	118.349
Translational	41.371
Rotational	31.010
Vibrational	45.969
Thermal energy	
Total	146.495
Translational	0.889
Rotational	0.889
Vibrational	144.718
Heat capacity	
Total	50.332
Translational	2.981
Rotational	2.981
Vibrational	44.370
Dipole moment	
μ_x	4.056
μ_y	0.057
μ_z	-1.699
μ	4.398

respectively. Molecular electrostatic potential, V(r) is the resultant at each point r, which is the net electrostatic effect produced at the point r by both the electrons and nuclei of the molecule.

Molecular electrostatic potential (MEP) is an important tool used to predict the reactivity of a wide variety of chemical systems in both electrophilic and nucleophilic reactions [41, 42]. It provides a visual method to understand the relative polarity of the molecule. Fig. 10 shows the MEP surface plot for the molecule computed at B3LYP/6-311G (d,p) level on the optimized geometry of the molecule. The electrostatic potential ranges from -0.0297 to +0.0297 a. u. with deepest blue density

https://doi.org/10.1016/j.heliyon.2019.e01574

which represents the electron deficient regions V(r) > 0.0297 a. u.) and deepest red density represents the electron rich regions (V(r) < -0.0297a.u.) in the plot. The maximum values of ESP show that the C7 carbons and hydrogen are acidic, exhibit greater positive potentials ~18.4942eV. The green area represents the zero electrostatic potential regions. It is seen from Fig. 10 that the region around oxygen atom (O10) linked with carbon through double bond represents the most negative potential region (red) and the region around the hydrogen atom represents the maximum positive charge (blue) in molecule. The predominance of light green region in the MEP surfaces corresponds to a potential halfway between the two extremes red and dark blue color.

The calculated thermo-dynamical parameters are presented in Table 7 such as total energy, zero-point vibrational energy, rotational constants and entropy at room temperature using B3LYP/6-311++G (d, p) basis set. Thermodynamic parameters can explain the stability and reactivity of a molecule. As seen from the table, total energy and total thermal energy of GLV is -610.564 a.u and 146.495 cal mol^{-1} K^{-1}respectively. Additionally, it is found that the total entropy and heat capacity of GLV is 118.349 and 50.332 cal mol^{-1} K^{-1}. Furthermore, dipole moment, which is an important value helping to characterize the electronic property of a molecule by atomic charge distribution.

5. Conclusion

Single crystals of organic GLV were grown by slow evaporation technique. Second harmonic generation efficiency of GLV is ~4.3 times greater than that of potassium dihydrogen orthophosphate. DFT based calculations with B3LYP/6.311+G(d,p) basis set reveal the delocalization of electron charge cloud due to stabilization of the carboxylate ion by resonance leading to the de-protonation of the carboxyl group and the subsequent protonation of the amino group. Further delocalization of charge cloud happens through C—H….O, N-H…..O and C —H……N bonds due to intermolecular hydrogen bond at the N-H sites which act as a channel for intermolecular charge transfer. The Hirshfeld surface analysis confirms the intermolecular interactions of GLV crystal. Such D-π-A systems in crystalline form having dense molecular packing serve as a good candidate for high mobility charge transport diode and field effect transistor.

Declarations

Author contribution statement

C. Usha: Conceived and designed the experiments; Performed the experiments; Wrote the paper.

https://doi.org/10.1016/j.heliyon.2019.e01574

R. Santhakumari: Analyzed and interpreted the data; Wrote the paper.

Lynnette Joseph, R. Meenakshi: Contributed reagents, materials, analysis tools or data.

D. Sajan, A. Sinthiya: Analyzed and interpreted the data.

Funding statement

C. Usha was supported by Management, Principal, J.J. College of Arts & Science (Autonomous), Sivapuram, Pudukkottai, and University Grants Commission New Delhi[File No. MRP 6165/2015 (CU)].

Competing interest statement

The authors declare no conflict of interest.

Additional information

No additional information is available for this paper.

Acknowledgements

Authors thank IIT Madras, Chennai, for extending laboratory facilities to record the FT-Raman spectrum. The authors thank CECRI, Karaikudi and Sastra University, Thanjavur, for extending the laboratory facilities to record the Powder XRD and NMR spectrum respectively.

References

[1] C.H. Bosshard, M. Bosch, I. Liakatas, M. Jager, P. Gunter, Springer Series in Optical Science, 72, Berline, Heideberg, New York, 2000, pp. 163−299.

[2] J. Zyss, J.F. Nicoud, M. Coquillay, Chirality and hydrogen bonding in molecular crystals for phase-matched second-harmonic generation: N-(4-nitrophenyl)-(L)-prolinol (NPP), J. Chem. Phys. 81 (9) (1984) 4160−4167.

[3] M. Ravi, P. Gangopadhyay, D.N. Rao, S. Cohen, I. Aganat, T.P. Radhakrishnan, Dual influence of H-bonding on the solid-state second-harmonic generation of a chiral quinonoid compound, Chem. Mater. 10 (9) (1998) 2371−2377.

[4] H.A. Petrosyan, H.A. Karapetyan, M. Yu. Antipin, A.M. Petrosyan, Nonlinear optical crystals of l-histidine salts, J. Cryst. Growth 275 (1−2) (2005) 1919−1925.

https://doi.org/10.1016/j.heliyon.2019.e01574

[5] M. Lydia Caroline, R. Sankar, R.M. Indirani, S. Vasudevan, Growth, optical, thermal and dielectric studies of an amino acid organic nonlinear optical material: l-Alanine, Mater. Chem. Phys. 114 (1) (2009) 490–494.

[6] P. Anandan, M. Arivanandhan, Y. Hayakawa, D. RajanBabu, R. Jayavel, G. Ravi, G. Bhagavannarayana, Investigations on the growth aspects and characterization of semiorganic nonlinear optical single crystals of l-histidine and its hydrochloride derivative, Spectrochim. Acta 121 (2013) [508]–[513].

[7] S. Masilamani, A. Mohamed Musthafa, Chemical analysis, FTIR and microhardness study to find out nonlinear optical property of l-asparagine lithium chloride: a semiorganic crystal, Microchem. J. 110 (2013) 749–752.

[8] T. Mallik, T. Kar, Growth and characterization of nonlinear optical l-arginine dihydrate single crystals, J. Cryst. Growth 285 (1–2) (2005) 178–182.

[9] G. Ravichandran, S. Arumugam, T.K. Nambi-narayanan, Ultrasonic velocity and absorption studies on some amino acids in water-aprotic solvent mixtures, J. Pure Appl. Ultrason. 34 (2012) 17–21.

[10] M. Fleck, A.M. Petrosyan, Salts of Amino Acids, Springer International Publishing, Switzerland, 2014.

[11] K. Srinivasan, Crystal growth of α and γ glycine polymorphs and their polymorphic phase transformations, J. Cryst. Growth 311 (1) (2008) 156–162.

[12] A. Lehninger, Principles of Bio Chemistry, Worth publishers inc., New York, 1984.

[13] C.H. Görbitz, S. Agustsdottir, F. Bleken, Pearls on a string: a$Z' = 7$ structure for glycyl-L-valine, Acta Cryst. C 63 (1) (2007) o58–o60.

[14] M.K. Marchewka, A. Pietraszko, Crystal structure and vibrational spectra of piperazinium bis(4-hydroxybenzenesulphonate) molecular–ionic crystal, Spectrochim. Acta A Mol. Biomol. Spectrosc. 69 (2) (2008) 312–318.

[15] R.M. Silverstein, F.X. Webster, Spectrometric Identification of Organic Compounds, sixth ed., Wiley, New York, USA, 1998.

[16] S.K. Kurtz, T.T. Perry, A powder technique for the evaluation of nonlinear optical materials, J. Apply. Phys. 39 (8) (1968) 3798–3813.

[17] S.K. Wolff, D.J. Grimwood, J.J. McKinnon, M.J. Turner, D. Jayatilaka, M.A. Spackman, CrystalExplorer, University of Western Australia, 2012, Version 3.1.

[18] G. Socrates, Infrared and Raman Characteristics Group Frequencies, Wiley, New York, USA, 2000.

https://doi.org/10.1016/j.heliyon.2019.e01574

[19] R.M. Silverstein, G.C. Basseler, C. Morrill, Spectrometric Identification of Organic Compounds, John Wiley, New York, USA, 1991.

[20] C.B. Smith, Infrared Spectral Interpretation, CRC Press, New York, USA, 1999.

[21] L.J. Bellamy, The Infrared Spectra of Complex Molecules, Methuen and Co., London, 1956.

[22] G.B.B.M. Sutherland, Infrared analysis of the structure of amino acids, polypeptides and proteins, Adv. Protein Chem. 7 (1952) 291−318.

[23] R.J. Koegel, J.P. Greenstein, M. Winitz, S.M. Birnbaum, R.A. McCallum, Studies on diastereoisomeric α-amino acids and corresponding α-hydroxy acids. V. Infrared spectra, J. Am. Chem. Soc. 77 (21) (1955) 5708−5720.

[24] H. Torii, T. Tatsumi, M.J. Tasumi, Effects of hydration on the structure, vibrational wavenumbers, vibrational force field and resonance raman intensities of N-methylacetamide, Raman Spectrosc. 29 (1998) 537−546.

[25] P. Schmidt, J. Dybal, J. C Rodriguez-Cabello, V. Reboto, Role of water in structural changes of poly(AVGVP) and poly(GVGVP) studied by FTIR and Raman spectroscopy and ab initio calculations, Biomacromolecules 6 (2) (2005) 697−706.

[26] N.A. Besley, Ab initio modeling of amide vibrational bands in solution, J. Phys. Chem. A 108 (49) (2004) 10794−10800.

[27] N. B Colthup, L.H. Daly, S.E. Wiberley, Introduction to Infrared and Raman Spectroscopy, Academic Press, New York, USA, 1990.

[28] E.D. Glendening, A.E. Reed, J.E. Carpenter, F. Weinhold, NBO Version 3.1; T.C.I., University of Wisconsin, Madison, 1999.

[29] J. Liu, et al., High mobility emissive organic semiconductor, Nat. Commun. 6 (2015) 10032.

[30] Z. Zhou, R.G. Parr, Activation hardness: new index for describing the orientation of electrophilic aromatic substitution, J. Am. Chem. Soc. 112 (15) (1990) 5720−5724.

[31] J. Gilman, Chemical and physical “hardness”, J. Mater. Res. Innov. 1 (2) (1997) 71−76.

[32] J. Aihara, Reduced HOMO−LUMO gap as an index of kinetic stability for polycyclic aromatic hydrocarbons, J. Phys. Chem. A 103 (37) (1999) 7487−7495.

https://doi.org/10.1016/j.heliyon.2019.e01574

[33] J. Aihara, Why are some polycyclic aromatic hydrocarbons extremely reactive? Phys. Chem. Chem. Phys. 1 (14) (1999) 3193−3197.

[34] J. Aihara, Weighted HOMO-LUMO energy separation as an index of kinetic stability for fullerenes, Theor. Chem. Acc. 102 (1999) 134−138.

[35] R.G. Parr, P.K. Chattaraj, Principle of maximum hardness, J. Am. Chem. Soc. 113 (5) (1991) 1854−1855.

[36] R.G. Pearson, Absolute electronegativity and absolute hardness of Lewis acids and bases, J. Am. Chem. Soc. 107 (24) (1985) 6801−6806.

[37] R.G. Parr, R.G. Pearson, Absolute hardness: companion parameter to absolute electronegativity, J. Am. Chem. Soc. 105 (26) (1983) 7512−7516.

[38] T. Koopmans, Uber die Zuordnung von Wellenfunktionen and Eigenwerten zu den einzelnen Elektronen eines Atoms, Physica 1 (1934) 104−113.

[39] A. Rauk, Orbital Interaction Theory of Organic Chemistry, second ed., John Wiley & Sons, Newyork, 2001.

[40] J.S. Murray, K. Sen, Molecular Electrostatic Potentials, Concepts and Applications, Elsevier, Amsterdam, 1996.

[41] E. Scrocco, J. Tomasi, Electronic molecular structure, reactivity and intermolecular forces: an euristic interpretation by means of electrostatic molecular potentials, Adv. Quant. Chem. 11 (1978) 115−193.

[42] F.J. Luque, J.M. Lopez, M. Orozco, Perspective on "Electrostatic interactions of a solute with a continuum. A direct utilization of ab initio molecular potentials for the prevision of solvent effects", Theor. Chem. Acc. 103 (3−4) (2000) 343−345.

https://doi.org/10.1016/j.heliyon.2019.e01574